Authors' responses to Referees' comments

Journal: Atmospheric Measurement Techniques (AMT)

Manuscript Number: EGUSPHERE-2026-2017

Title: Enhanced discrimination of vertical aerosol types based on multiwavelength Mie–Raman–fluorescence lidar at a high-altitude background site

Authors: Yutong Tian, Ting Yang, et al.

Note：

Comment (16-point black italicized font).

Reply (indented, 16-point blue normal font).

"Revised text as it appears in the text (in quotes, 16-point blue italicized font)".

Anonymous Referee #1

1 Summary:

Authors present approach for analysis of aerosol mixture in troposphere based on observations Mie-Raman-fluorescence lidar. This is important task, but I think that manuscript needs significant revision. In particular, I am surprised, that authors don't provide any profile of particle parameters measured by lidar. This is important to prove the quality of observations. Choice of particle parameters for every aerosol type needs also strong discussion. Citation list is incomplete.

Authors' response:

We sincerely thank the reviewer for recognizing the importance of this study and for providing constructive comments. We have carefully considered the reviewer's overall concerns and have substantially revised the manuscript. The main revisions are summarized below.

(1). Regarding the lack of lidar-retrieved particle-parameter profiles:

In response to the reviewer's concern that the original manuscript did not provide lidar-retrieved particle-parameter profiles, we have added representative seasonal vertical profiles for the four seasons of 2023 in the revised manuscript and Supplementary Material (Figure Rs1). These profiles include the key lidar-measured and retrieved variables, namely fluorescence capacity, particle depolarization ratios, color ratios, lidar ratios, extinction coefficients, and backscatter coefficients (Figure Rs1). We also added a corresponding description of the seasonal mean optical profiles in Section 3.2.1. In addition, we included two representative time-height case studies in Section 3.3 (Figures Rs2-Rs3) to further illustrate how these optical parameters evolve with time and height, and how they jointly constrain aerosol-type decomposition. Detailed analyses of these cases are provided in our response to Comment 16.

Text added in Section 3.2.1 to describe the seasonal optical profiles (Figure Rs1):

"Figure S2 shows the seasonal mean vertical profiles of the seven optical parameters in 2023 together with their uncertainty ranges. The profiles reveal clear vertical stratification and seasonal variability of aerosols. In the vertical dimension, the rapid decrease of $Cr_{355/532}$ *with height and the rapid increase of the lidar ratios within the lowest 1 km indicate that relatively larger particles dominate in the lower atmosphere, whereas finer-mode aerosols become more important aloft. Meanwhile, the increasing Gf with height suggests enhanced contributions of specific biogenic or carbonaceous organic aerosol components in the upper layers. Seasonally, lower* $\delta532$ *and mid-to-upper-level Gf values in summer are likely related to high humidity and strong convection, whereas higher* δ_{355} *in winter and spring indicates increased contributions of nonspherical particles. Overall,* $Cr_{1064/532}$ *remains relatively stable throughout the year, suggesting that the overall coarse-mode versus fine-mode aerosol structure in this region does not vary drastically among seasons."*

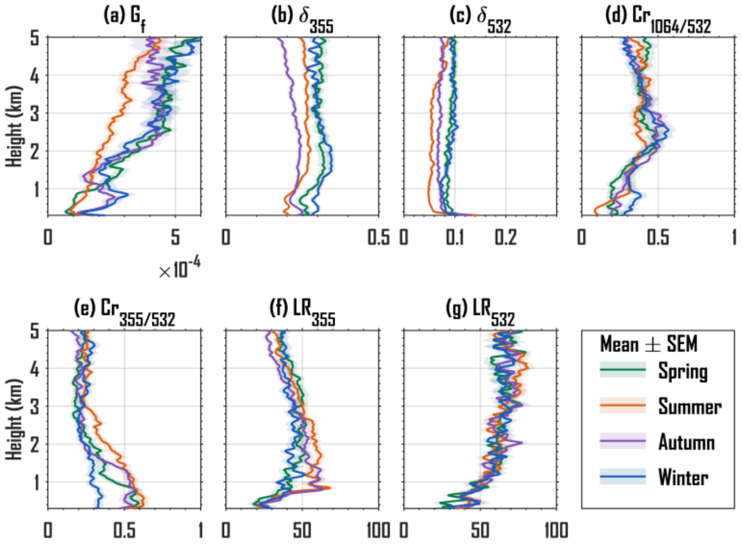

Figure Rs1. Seasonal vertical profiles of the seven optical parameters.

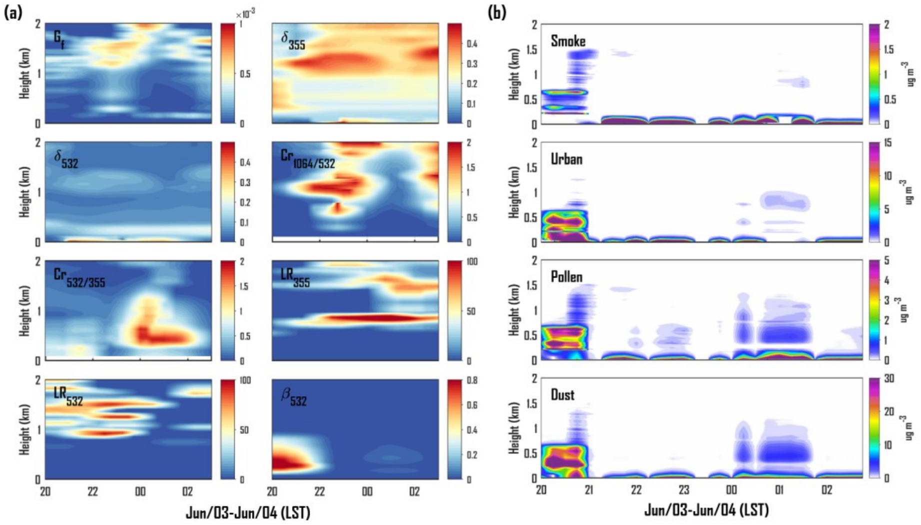

Figure Rs2. Time-height cross-sections of the optical parameters (a) and aerosol mass concentrations (b) on 3-4 June 2023.

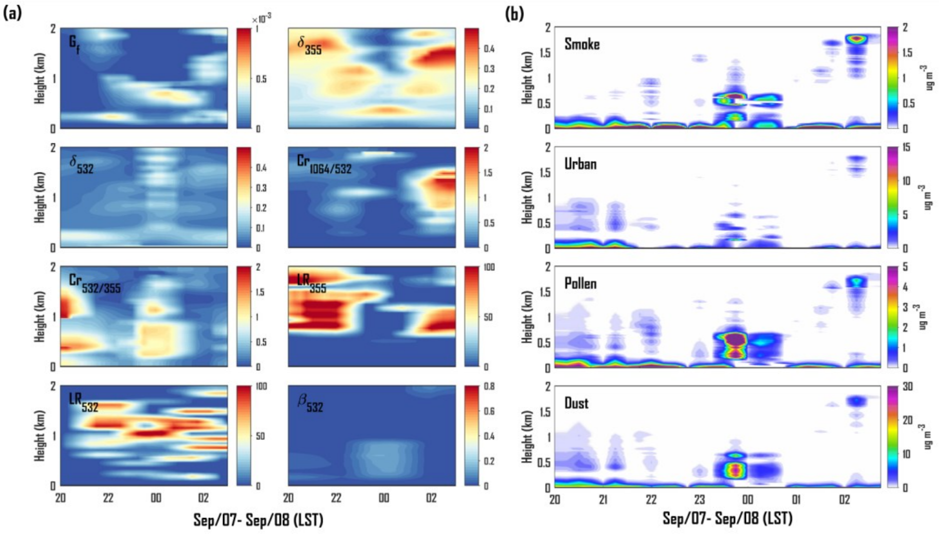

Figure Rs3. Same as Figure Rs2, but for 7-8 September 2023.

(2). Regarding the selection of particle parameters for each aerosol type:

For the selection of particle-parameter ranges, we substantially strengthened the discussion of the parameter-selection framework in Section 2.2. In the revised manuscript, we now explicitly state that the reference intervals were derived from published lidar studies rather than fitted from the observations in this study: "*The reference intervals shown in Fig. 1 were not obtained by fitting the observations in this study; instead, they were compiled from published lidar studies and are used as prior constraints in the classification algorithm. Table S1 in the Supplement provides the* *detailed literature sources for each aerosol type and each parameter.*" In addition, we included an independent comparison with the DeLiAn database (Floutsi et al., 2023) to assess whether the lidar-intensive parameters overlapping with this study are consistent with previously reported statistical ranges (Figure Rs4). The remaining differences are further discussed in terms of regional variability, aerosol-type definitions, and wavelength configuration, as detailed in our response to Comment 4.

For the pollen-related parameters, we further clarified the environmental background of the observation site and explicitly stated in the revised Section 2.2 that these parameters mainly represent local tree pollen associated with the broadleaf and coniferous forest environment surrounding ABLES. We also compared the adopted pollen-parameter ranges with those reported in the laboratory and atmospheric pollen lidar studies recommended by the reviewer (Figure Rs5), including Cholleton et al. (2022) and Shang et al. (2020), as detailed in our response to Comment 6.

For the selection of the smoke LR_{532} range, we revised the interval from 30-85 sr to 45-85 sr based on the DeLiAn database. This modification better reflects the characteristic that the lidar ratio of smoke at 532 nm is generally higher than that at 355 nm, as addressed in our response to Comment 8.

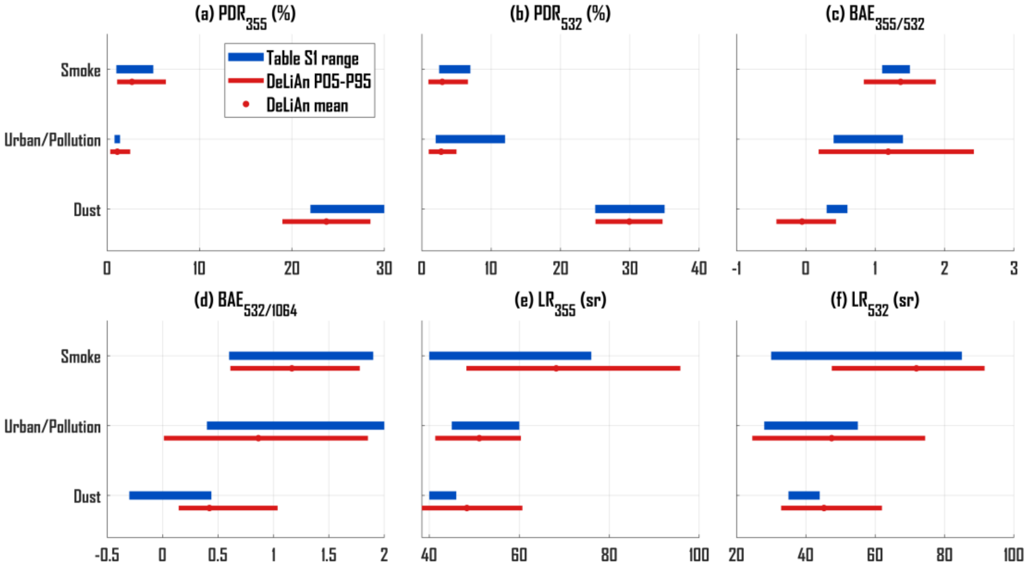

Figure Rs4. Comparison between the literature-derived reference ranges used in this study and the DeLiAn database statistics for overlapping lidar intensive parameters.

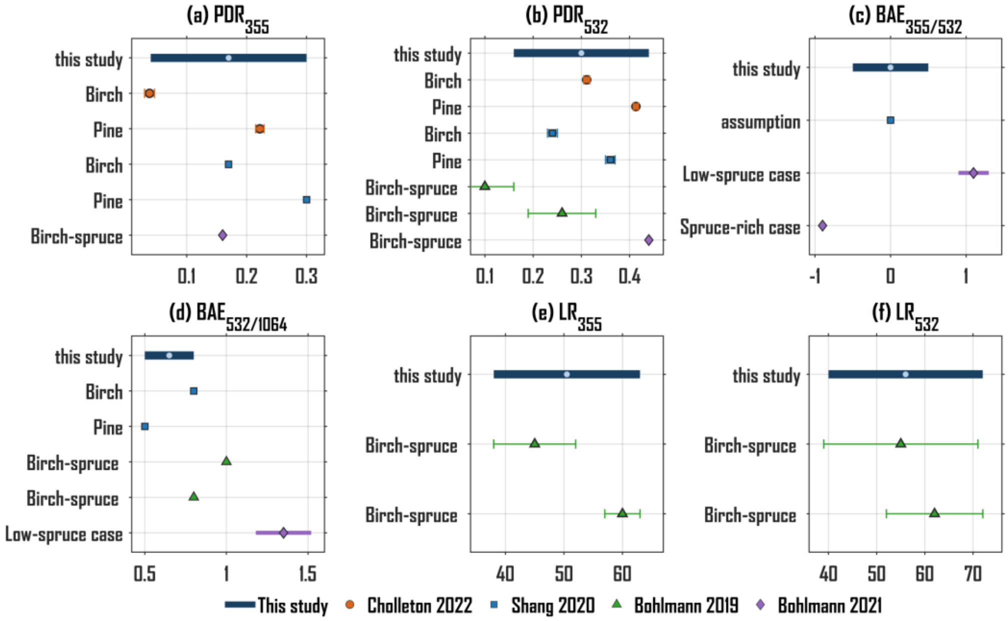

Figure Rs5. Comparison between the corrected pollen classification ranges used in this study and the cited literature values.

(3). Regarding the incomplete citation list:

Regarding the incomplete citation list, we added several relevant references in the revised manuscript. First, in Section 2.2 (around Line 120), we added citations to previous studies by Burton et al. on aerosol mixture analysis, as addressed in our response to Comment 3. Second, for the pollen depolarization-ratio range, we added the reference by Cholleton et al. (2022) in Lines 155-158, as detailed in our response to Comment 6. Third, for the extinction-to-volume conversion factors, we added the relevant references in Line 170, including Mamouri and Ansmann (2017), He et al. (2023), and Ansmann et al. (2019), as addressed in our response to Comment 9. These additions improve the completeness of the reference list and better support the methodological basis of the study.

Overall, we have substantially revised the manuscript in response to the reviewer's summary comments. We believe that the revised version now more clearly documents the observational basis of the lidar products, provides a stronger and more transparent justification for the selected aerosol optical parameters, and presents the methodology in a more complete and well-supported form.

2 specific comments:

1) Table 1. Some information is not necessary, for example, lamp lifetime. If photon counting rate is up to 20 MHz, dead-time correction procedure should be mentioned (cited).

Authors' response:

Table 1 has been revised by updating and simplifying the listed system parameters, retaining only the information directly relevant to lidar signal acquisition, system performance, and retrieval analysis (Table R1). In response to the reviewer's concern about the photon-counting rate, we have also added a detailed description of the dead-time correction procedure. Our detailed response and the corresponding revisions made in Section 2.1 are provided below.

The photon-counting channels of our lidar system use Hamamatsu H10720/H10721 series metal-package PMT photosensor modules. According to the response characteristics of this type of PMT module, the effective dead time is approximately 2-3 ns. Therefore, in the data processing, the photon-counting signals were corrected using a non-paralyzable photon-counting model with τ = 2-3 ns. The correction factor was calculated bin by bin from the single-shot, single-bin count N' (Donovan et al., 1993; Rodriguez-Gomez et al., 2015):

$$CF = \frac{1}{\left[1 - \frac{N'\tau}{t_{bin}}\right]} \tag{R1}$$

and the corrected count was obtained as:

$$N_{true} = N_{obs} \times CF \tag{R2}$$

where t_{bin} is the time window of a single range bin.

Using the adopted PMT dead-time range of τ = 2-3 ns, the resulting correction factors are close to unity for typical signal levels. The median correction factors are approximately 1.0000-1.0015 for all channels. At the 95th-percentile signal level, the correction factors are generally about 1.0046-1.0141 for most channels, while the 1064 nm elastic channel (E_{1064}) reaches approximately 1.0363-1.0555 because of its higher count level. These values indicate that the dead-time correction is very small for typical signal levels and becomes noticeable mainly at the high-count-rate end, especially for E1064. We have added the PMT type, the adopted dead-time value, and the corresponding correction procedure in Section 2.1 of the revised manuscript.

Table R1. Main Parameters of the Lidar System

Definition	**Reference value**
Operating wavelengths	355 nm / 532 nm / 1064 nm
Maximum pulse repetition frequency	10 Hz
Pulse width	< 10 ns
Measurement distance	10 km
Number of detection / receive channels	8
Filter bandwidth (peak / FWHM)	≤ 1 nm
Filter bandwidth (fluorescence)	44 nm
Effective PMT dead time	2-3 ns
Photon-counting sampling rate	> 20 MHz
Spatial resolution	15 m

Text added in Section 2.1, around Line 100:

"Before aerosol optical retrieval, the photon-counting signals were corrected for dead-time effects. The photon-counting channels of the lidar system use Hamamatsu H10720/H10721 series metal-package PMT photosensor modules. Based on the response characteristics of this PMT module, an effective dead-time range of 2-3 ns was adopted. The correction was performed using a non-paralyzable photon-counting model, in which the correction factor was calculated for each range bin as：

$$CF = \frac{1}{\left[1 - \frac{N'\tau}{t_{bin}}\right]}, \tag{1}$$

where N' *is the single-shot photon count in each range bin,* τ *is the assumed dead time, and* t_{bin} *is the time window corresponding to one range bin. The corrected photon count was then obtained as:*

$$N_{true} = N_{obs} \times CF. \tag{2}$$

For the adopted dead-time range of 2-3 ns, the correction factors were close to *unity for most observed signal levels, indicating that the influence of dead-time correction on the subsequent retrieval was generally small, although it became more noticeable for high-count-rate channels. This treatment follows the standard non-paralyzable photon-counting correction approach used in lidar signal processing (Donovan et al., 1993; Rodríguez-Gómez et al., 2015).”*

References

Donovan, D. P., Whiteway, J. A., and Carswell, A. I.: Correction for nonlinear photon-counting effects in lidar systems, Appl. Opt., 32, 6742-6753, 10.1364/AO.32.006742, 1993.

Rodríguez-Gómez, A., Rocadenbosch, F., Sicard, M., Lange, D., Barragán, R., Batet, O., Comerón, A., Márquez, M. A. L., Muñoz-Porcar, C., Tiana, J., and Tomás, S.: Multi-wavelength aerosol LIDAR signal pre-processing: practical considerations, IOP Conference Series: Earth and Environmental Science, 28, 012013, 10.1088/1755-1315/28/1/012013, 2015.

2) Ln.105 “For the elastic (Mie) channels, aerosol optical parameters are retrieved using the Fernald algorithm (Fernald, 1984)…” Authors measure Raman signals but use Fernald method. Should be explained why.

Authors’ response:

We thank the reviewer for this insightful comment, which provided valuable guidance for improving the internal consistency of our retrieval framework. In the original implementation, the algorithm was designed as a combined Mie-Raman-fluorescence framework, in which Raman signals were used as important observational constraints, while the Fernald-derived 532 nm extinction was retained in the fluorescence-channel transmission correction as part of the complete combined-retrieval structure. This design was mainly intended to maintain consistency with the conventional elastic-lidar retrieval branch and to provide a practical transmission correction for the fluorescence channel.

Inspired by the reviewer’s suggestion, we carefully reconsidered this mixed treatment and revised the subsequent retrieval algorithm to make the 355 and 532 nm optical products more consistently based on Raman constraints. The corresponding descriptions in the manuscript have also been updated. Accordingly, the algorithm workflow, parameter retrievals, result presentation, and case analyses related to this method have been revised consistently throughout the manuscript to reflect the changes described above. The detailed response and the revised manuscript text are provided below.

In the updated workflow, the extinction coefficients at 355 and 532 nm are retrieved independently from the Raman channels, and the corresponding backscatter products at these two wavelengths are also obtained under Raman constraints. Most importantly, the fluorescence-channel transmission correction, which in the original version used the Fernald-derived 532 nm extinction, has now been replaced by the extinction retrieved directly from the Raman channel. Therefore, the extinction, backscatter, and fluorescence-related products at 355 and 532 nm that are used for aerosol classification and quantitative analysis are now consistently based on a Raman-only framework, without relying on an assumed Fernald lidar ratio.

The Fernald method is now retained only for the auxiliary 1064 nm elastic branch, because the present system does not provide a corresponding Raman channel at this wavelength. In the revised algorithm, this branch is used only to provide the 1064 nm backscatter information needed for the long-wavelength color-ratio constraint.

We have revised the manuscript accordingly to state clearly that the original dependence of the fluorescence retrieval on the Fernald method has been removed, and that the Fernald method is now used only in the auxiliary 1064 nm branch. Correspondingly, the fluorescence-retrieval flowchart previously shown in Fig. S1 has been updated and is now presented as Figure R2. Because of this methodological revision, the final aerosol mass-concentration results originally shown in Fig. 5 have also been updated, as presented in Figure R3. In addition, the validation against ground-based PM measurements has been updated and is now presented in Figure R7, while the related case analyses have also been revised accordingly and are now shown in

Figures R8 and R10.

Text revised in Section 2.1, Lines 103-119, as follows:

"Photon-counting signals acquired by the lidar system first undergo preprocessing, including background subtraction, dead-time correction, overlap correction, and range-square correction. Preliminary retrievals are subsequently conducted based on these pre-processed data (Fig. S1b). For the Raman channels, aerosol extinction coefficients at 355 and 532 nm are retrieved independently by exploiting the combined attenuation relationship of the Raman scattering echoes at both the laser and Raman wavelengths. This approach circumvents the need for aerosol lidar ratio assumptions, thereby reducing dependence on prior information and minimizing systematic uncertainties (Ortiz-Amezcua et al., 2020; Zhao et al., 2021). The corresponding aerosol backscatter coefficients at 355 and 532 nm are then obtained under Raman constraints. For the fluorescence channel, the path transmittance correction is calculated using the Raman-derived extinction coefficients. The Ångström power law is applied to extrapolate the Raman-derived extinction coefficients to the wavelengths of the fluorescence and Raman channels for the calculation of atmospheric transmittance. Based on this Raman-constrained transmittance correction, the fluorescence backscatter coefficient (β_F) is retrieved from the fluorescence and Raman signals. This methodology is consistent with recent developments in multichannel Raman-fluorescence lidar observations and algorithm applications (Veselovskii et al., 2020; Gast et al., 2025; Huang et al., 2025).

The Fernald algorithm (Fernald, 1984) is used only for the auxiliary 1064 nm elastic channel, because the present lidar system does not provide a corresponding Raman channel at this wavelength. This branch provides the long-wavelength backscatter information required for the color-ratio constraint and is not used for the fluorescence-channel transmission correction. Data from the Raman and fluorescence channels exhibit high reliability at night owing to robust signal-to-noise ratios but are sensitive to background light during daytime. Therefore, this study exclusively utilizes observations from April to December 2023, restricted to the hours of 18:00 LST to

07:00 LST the following day, to guarantee data reliability."

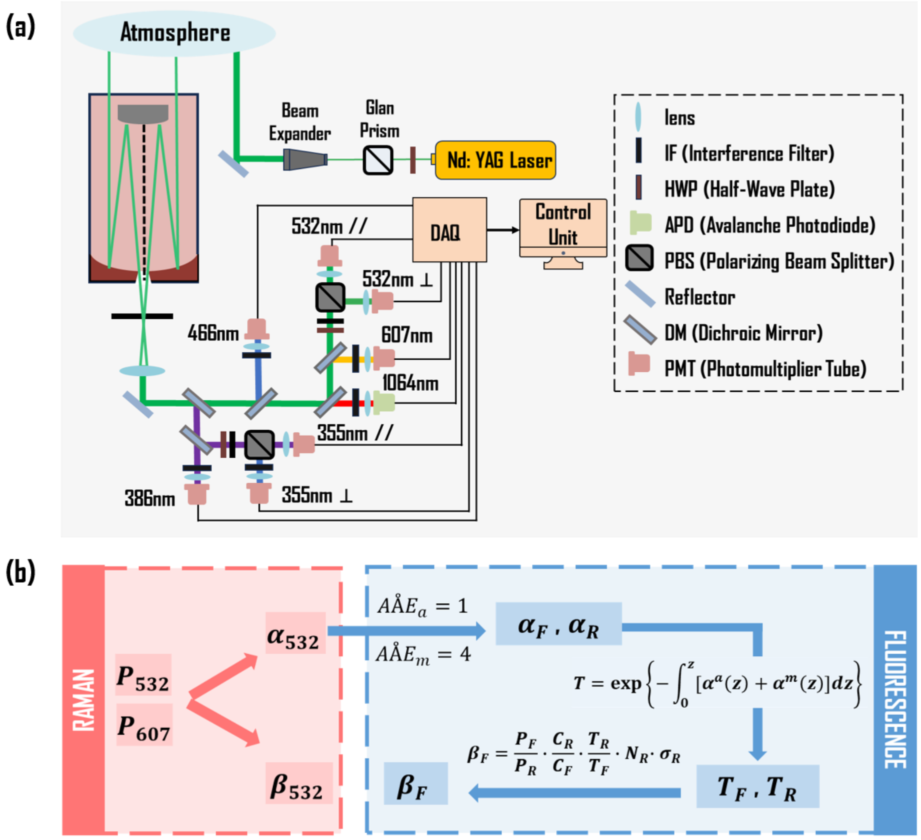

Figure R2. Overview of the multiwavelength Mie-Raman-fluorescence lidar system. (a) Schematic diagram of the instrument configuration. (b) Flowchart of the revised Raman-only and fluorescence retrieval workflow.

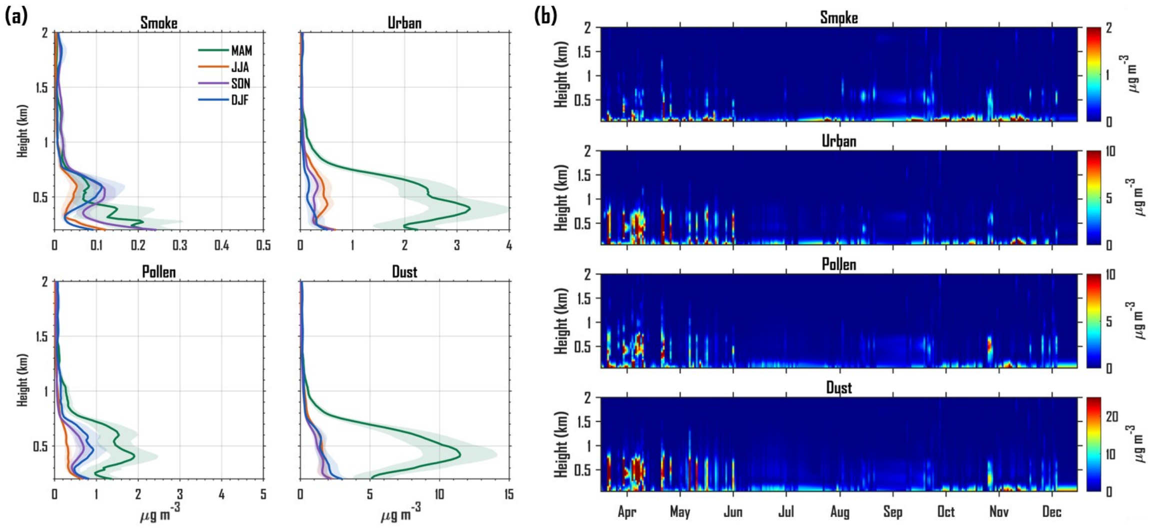

Figure R3. Revised aerosol mass-concentration results: (a) seasonal profiles of the four aerosol

components; (b) time-height sections of aerosol mass concentration from April to December.

3) Section 2.2. I would recommend to cite some works of Burton et al., on mixture analysis. For example:

Burton, S. P., Ferrare, R. A., Hostetler, C. A., Hair, J.W., Rogers, R. R., Obland, M. D., Butler, C. F., Cook, A. L., Harper, D. B., and Froyd, K. D.: Aerosol classification using airborne High Spectral Resolution Lidar measurements – methodology and examples, Atmos. Meas. Tech., 5, 73–98, 2012. https://doi.org/10.5194/amt-5-73-2012

Burton, S. P., Ferrare, R. A., Vaughan, M. A., Omar, A. H., Rogers, R. R., Hostetler, C. A., and Hair, J. W.: Aerosol classification from airborne HSRL and comparisons with the CALIPSO vertical feature mask, Atmos. Meas. Tech., 6, 1397–1412, 2013. https://doi.org/10.5194/amt-6-1397-2013

Burton, S. P., Vaughan, M. A., Ferrare, R. A. and Hostetler, C. A.: Separating mixtures of aerosol types in airborne High Spectral Resolution Lidar data. Atmos. Meas. Tech. 7, 419-436, 2014. DOI: 10.5194/amt-7-419-2014

Burton, S. P., Hair, J. W., Kahnert, M., Ferrare, R. A., Hostetler, C. A., Cook, A. L., Harper, D. B., Berkoff, T. A., Seaman, S. T., Collins, J. E., Fenn, M. A., and Rogers, R. R.: Observations of the spectral dependence of linear particle depolarization ratio of aerosols using NASA Langley airborne High Spectral Resolution Lidar, Atmos. Chem. Phys., 15, 13453–13473, 2015 doi:10.5194/acp-15-13453-2015.

Authors' response:

The suggested studies by Burton et al. provide important methodological background for lidar-based aerosol classification and mixture analysis. We have cited these works in Section 2.2 and slightly revised the text to acknowledge their contributions to multi-parameter aerosol typing and mixture separation.

Text added in Section 2.2, around Line 120:

"*Lidar-based aerosol classification and mixture analysis have been extensively* *investigated using multi-parameter optical constraints from High Spectral Resolution Lidar (HSRL) observations. Burton et al. (2012, 2013) demonstrated aerosol classification based on lidar-derived intensive optical properties, and Burton et al. (2014) further developed a method for separating mixtures of aerosol types in airborne HSRL data. The spectral dependence of the particle depolarization ratio also provides additional constraints for aerosol-type discrimination (Burton et al., 2015). Building on this general multi-parameter classification concept, we developed a multiparameter constrained algorithm for multiwavelength Mie-Raman-fluorescence lidar observations by incorporating fluorescence capacity, dual-wavelength depolarization ratios, lidar ratios, and backscatter-related spectral parameters."*

4) Fig.1. Should be explained how these values were obtained. Intensive parameters of aerosols were reported in numerous publications of NASA Langley group, TROPOS group and within EARLINET. I would recommend to provide discussion and compare presented results with previous findings.

Floutsi, A. A., Baars, H., Engelmann, R., Althausen, D., Ansmann, A., Bohlmann, S., Heese, B., Hofer, J., Kanitz, T., Haarig, M., Ohneiser, K., Radenz, M., Seifert, P., Skupin, A., Yin, Z., Abdullaev, S. F., Komppula, M., Filioglou, M., Giannakaki, E., Stachlewska, I. S., Janicka, L., Bortoli, D., Marinou, E., Amiridis, V., Gialitaki, A., Mamouri, R.-E., Barja, B., and Wandinger, U.: DeLiAn – a growing collection of depolarization ratio, lidar ratio and Ångström exponent for different aerosol types and mixtures from ground-based lidar observations, Atmos. Meas. Tech., 16, 2353–2379, https://doi.org/10.5194/amt-16-2353-2023, 2023a.

Authors' response:

We agree that the origin of the intensive-parameter ranges shown in Fig. 1 was not sufficiently explained in the original manuscript. We now provide a detailed explanation of how these ranges were obtained and added an independent comparison with the DeLiAn database of Floutsi et al. (2023). The corresponding clarification and discussion have been added to the revised manuscript as follows.

The parameter ranges shown in Fig. 1 were not derived from fitting the observations in this study. Instead, they were compiled from previously published lidar studies and were used as literature-based prior intervals in our classification and retrieval framework. The corresponding source references for each aerosol type and parameter were provided in Table S1. To make the construction of Fig. 1 clearer, we have now explicitly clarified the relationship between Fig. 1 and Table S1 in the revised manuscript.

To provide an independent evaluation of the selected parameter intervals, we compared the literature-based ranges used in this study with the DeLiAn database of Floutsi et al. (2023). DeLiAn compiles particle depolarization ratios, lidar ratios, and Ångström exponents for different aerosol types and mixtures from ground-based lidar observations, including results from EARLINET, TROPOS, and related international lidar studies. For the overlapping parameters, we used the 5th-95th percentile ranges reported in DeLiAn as the comparison reference. This comparison shows that, for most parameters, the intervals adopted in this study are broadly consistent with DeLiAn (Figure R4). Some differences remain for dust lidar ratios and backscatter-related Ångström exponents, which is expected because DeLiAn includes regional dust categories with different optical characteristics. Pollen and fluorescence capacity are not included as independent entries in DeLiAn. Therefore, for these parameters we continue to use the specialized pollen studies and Mie-Raman-fluorescence lidar studies listed in Table S1.

In the revised manuscript, we have clarified the literature-based origin of the Fig. 1 parameter ranges and added a supplementary comparison with the corresponding DeLiAn statistics, so that the construction and interpretation of these prior intervals are more transparent.

Revised text in Section 2.2 (Lines 120-160):

"The reference intervals shown in Fig. 1 were not obtained by fitting the observations in this study; instead, they were compiled from published lidar studies and are used as prior constraints in the classification algorithm. Table S1 in the Supplement

provides the detailed literature sources for each aerosol type and each parameter. These intervals cover the reported ranges of fluorescence capacity, particle depolarization ratio, color ratio, backscatter-related spectral dependence, and lidar ratio for smoke, urban/pollution aerosol, pollen, and dust.

To further evaluate the consistency of the adopted parameter intervals, we compared the parameters that overlap with the DeLiAn database (Fig. S4). DeLiAn summarizes ground-based lidar observations of depolarization ratio, lidar ratio, and Ångström exponent for different aerosol types and mixtures (Floutsi et al., 2023). The comparison shows that the intervals adopted here for smoke, urban/pollution aerosol, and dust are generally consistent with DeLiAn, while some dust-related differences mainly reflect regional variability in dust optical properties and differences in aerosol-type definitions, mixing states, and wavelength configurations."

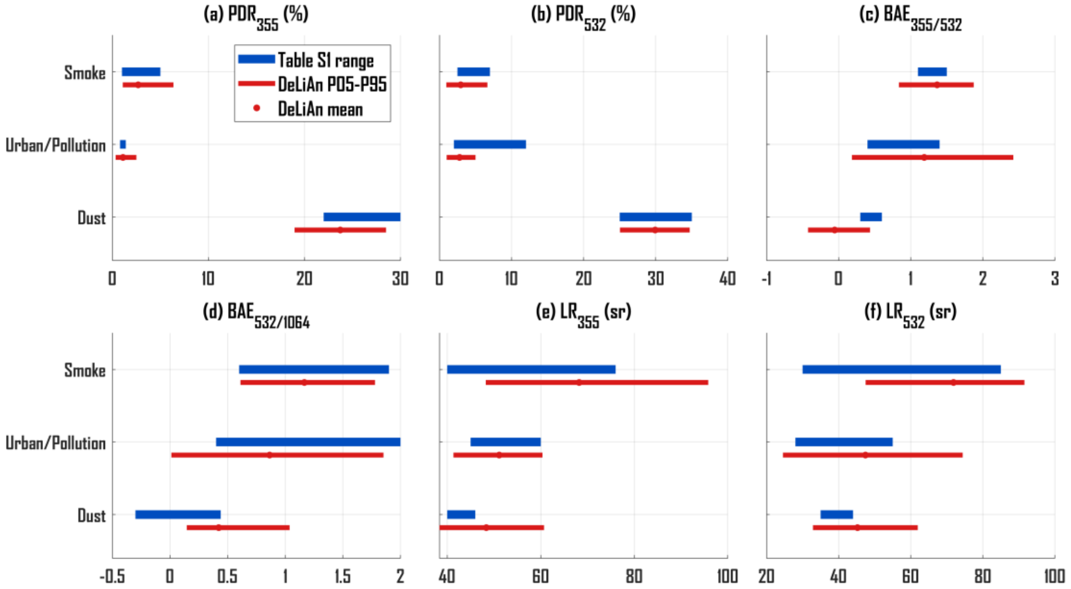

Figure R4. Comparison between the literature-derived reference ranges used in this study and the DeLiAn database statistics for overlapping lidar intensive parameters. Detailed source references for each parameter range are provided in Table S1.

5) (b). Usually, depolarization ratio of smoke at 355 is higher than at 532 (works of Hu et al, for example) In Table 1 it is opposite. Why?

Authors' response:

We acknowledge that several studies have reported higher smoke depolarization at 355 nm than at 532 nm, especially for aged wildfire smoke in the upper troposphere/lower stratosphere or stratosphere. For example, Hu et al. (2019) reported long-range-transported Canadian smoke in the lower stratosphere over northern France with PDR_{355} larger than 0.20 and PDR_{532} of about 0.18-0.19. Haarig et al. (2018) also reported strongly depolarizing stratospheric Canadian smoke, with PDR_{355} around 0.22 and PDR_{532} around 0.18. These observations support the reviewer's point that PDR_{355} can be higher than PDR_{532} for some smoke cases.

However, this wavelength dependence is not universal for all smoke aerosols. For tropospheric smoke, previous observations and aerosol databases show that PDR_{355} and PDR_{532} can be comparable, and PDR_{532} may even be slightly larger. Haarig et al. (2018) reported that the tropospheric Canadian smoke layer at 5-6.5 km produced very weak depolarization at 355, 532, and 1064 nm, with PDR values below about 3%; in that tropospheric case, no clear enhancement of PDR_{355} over PDR_{532} was observed. The DeLiAn database also supports this behavior. For the tropospheric smoke category, the mean PDR values are 2.7 ± 1.3% at 355 nm and 2.9 ± 0.6% at 532 nm, indicating comparable values with PDR_{532} slightly larger on average. In contrast, the stratospheric smoke category in DeLiAn shows much higher values and a different wavelength dependence, with $PDR_{355} = 22.6 \pm 4.0\%$ and $PDR_{532} = 17.9 \pm 1.7\%$.

Therefore, the apparent ordering in Table S1, PDR_{355} = 0.01-0.05 and PDR_{532} = 0.025-0.07, does not imply that smoke universally has lower depolarization at 355 nm than at 532 nm. Rather, it reflects the specific prior constraints adopted for tropospheric or long-range-transported smoke relevant to our high-altitude background site. These constraints are consistent with observations showing weak and comparable depolarization at 355 and 532 nm for tropospheric smoke.

To avoid ambiguity, we have added the following description of Table S1:

"*The PDR intervals for smoke are study-specific prior constraints for tropospheric or long-range-transported smoke relevant to this high-altitude background site. They should not be interpreted as universal depolarization ranges for all smoke aerosols.*"

Reference

De Rosa, B., Amodeo, A., D’Amico, G., Papagiannopoulos, N., Rosoldi, M., Veselovskii, I., Cardellicchio, F., Falconieri, A., Gumà-Claramunt, P., Laurita, T., Mytilinaios, M., Papanikolaou, C.-A., Amodio, D., Colangelo, C., Di Girolamo, P., Gandolfi, I., Giunta, A., Lapenna, E., Marra, F., Petracca Altieri, R. M., Ripepi, E., Summa, D., Volini, M., Arienzo, A., and Mona, L.: Characterization of Fresh and Aged Smoke Particles Simultaneously Observed with an ACTRIS Multi-Wavelength Raman Lidar in Potenza, Italy, 10.3390/rs17152538, 2025.

Floutsi, A. A., Baars, H., Engelmann, R., Althausen, D., Ansmann, A., Bohlmann, S., Heese, B., Hofer, J., Kanitz, T., Haarig, M., Ohneiser, K., Radenz, M., Seifert, P., Skupin, A., Yin, Z., Abdullaev, S. F., Komppula, M., Filioglou, M., Giannakaki, E., Stachlewska, I. S., Janicka, L., Bortoli, D., Marinou, E., Amiridis, V., Gialitaki, A., Mamouri, R. E., Barja, B., and Wandinger, U.: DeLiAn – a growing collection of depolarization ratio, lidar ratio and Ångström exponent for different aerosol types and mixtures from ground-based lidar observations, Atmos. Meas. Tech., 16, 2353-2379, 10.5194/amt-16-2353-2023, 2023.

Haarig, M., Ansmann, A., Baars, H., Jimenez, C., Veselovskii, I., Engelmann, R., and Althausen, D.: Depolarization and lidar ratios at 355, 532, and 1064 nm and microphysical properties of aged tropospheric and stratospheric Canadian wildfire smoke, Atmos. Chem. Phys., 18, 11847-11861, 10.5194/acp-18-11847-2018, 2018.

Hu, Q., Goloub, P., Veselovskii, I., Bravo-Aranda, J. A., Popovici, I. E., Podvin, T., Haeffelin, M., Lopatin, A., Dubovik, O., Pietras, C., Huang, X., Torres, B., and Chen, C.: Long-range-transported Canadian smoke plumes in the lower stratosphere over northern France, Atmos. Chem. Phys., 19, 1173-1193, 10.5194/acp-19-1173-2019, 2019.

6) Depolarization ratio of different pollen was studied in laboratory:

Cholleton, D.; Rairoux, P.; Miffre, A.: Laboratory evaluation of the (355, 532) nm particle depolarization ratio of pure pollen at 180.0 lidar backscattering angle. Remote Sens. 14, 3767, https://doi.org/10.3390/rs14153767, 2022.

Type of pollen should be specified and compared with previous findings

Authors' response:

Thank you for this valuable suggestion. We have more clearly explained the pollen type relevant to our study site in order to justify the selection of the depolarization-ratio range, and we have compared the adopted pollen optical parameters with related laboratory and atmospheric pollen studies.

The surrounding ecosystem of the study site is dominated by broadleaf and coniferous forests. Therefore, the pollen class used in this study is not intended to represent all pollen species, but mainly represents tree pollen relevant to the local broadleaf/coniferous forest environment. In the revised Supplement, we clarify that the pollen prior mainly represents local broadleaf/coniferous forest tree pollen, with birch-type and pine-type pollen used as the main literature references. We also corrected two pollen-related parameter entries in Table S1.

First, to include the relatively low 355 nm depolarization of birch pollen reported by Cholleton et al. (2022), the PDR_{355} interval was revised from 0.08-0.30 to 0.04-0.30. To make the literature basis of the revised parameter intervals clearer, we added Figure R5 to compare the corrected pollen classification ranges with the values reported in Table S1 and with the laboratory measurements of pure pollen suggested by the reviewer. The y-axis labels in Figure R5 specify the pollen type or observational/laboratory case, and the legend gives the corresponding literature source.

After revising PDR_{355} to 0.04-0.30, the adopted PDR range covers the laboratory birch and pine pollen values reported by Cholleton et al. (2022). The corrected $BAE_{532/1064}$ interval is consistent with the birch and pine values reported by Shang et al. (2020), and the revised $BAE_{355/532}$ interval is also consistent with the near-zero values reported in previous pollen studies. The adopted lidar-ratio range is broadly consistent with the atmospheric birch and birch-spruce pollen observations reported by Bohlmann et al. (2019). Overall, the revised intervals are appropriate as a local broadleaf/coniferous forest tree-pollen prior for the ABLES site.

At the same time, we further clarified the limitation of this pollen class in the revised manuscript. Because pollen optical properties are species-dependent, the pollen parameters in Table S1 should not be interpreted as universal parameters for all pollen species, nor should they be directly generalized to herbaceous pollen, crop pollen, or pollen types in other ecological regions. Applications to other sites or vegetation backgrounds would require additional constraints from local pollen composition and independent observations.

Revised text around Lines 155-158:

"*For the pollen category, we further clarify that the adopted parameters are intended to approximate representative tree-pollen optical properties relevant to the local broadleaf/coniferous forest environment around ABLES, rather than to cover the full diversity of all possible pollen species. ABLES is located on Mt. Damaojian in Wuyi County, Zhejiang Province, where broadleaf and coniferous forests are common in the surrounding mountain ecosystem. Therefore, the selection of the pollen optical parameter ranges was mainly based on literature concerning birch-type and pine-type pollen, including Cholleton et al. (2022), Shang et al. (2020), and Bohlmann et al. (2019, 2021). We compared the pollen classification ranges adopted in this study with the typical values reported in previous laboratory and atmospheric pollen lidar studies (Figure R5). The results show that the intervals of* PDR_{355}, $BAE_{355/532}$, $BAE_{532/1064}$, *and lidar ratio are generally consistent with the typical values reported for birch and pine pollen in previous studies, and are therefore appropriate as a local broadleaf/coniferous forest tree-pollen prior for the ABLES site.*"

Table R2. Corrected literature-based classification ranges of seven macroscopic optical parameters for smoke, urban/pollution aerosol, pollen, and dust.

Type	G_{F} (10^{-4})	PDR_{355}	PDR_{532}	$B\mathring{A}E_{532/1064}$	$B\mathring{A}E_{355/532}$	LR_{355}	LR_{532}
Smoke	2.5–4.5[a]	0.01–0.05[b, c]	0.025–0.07[d, e]	1.1–1.5[e, f]	0.6–1.9[e, f]	40–76[b-e]	**45–85[b-e]**
Urban	0.2–0.8[a]	0.008–0.014[c, g]	0.02–0.12[c]	0.4–1.4[c]	0.4–2.0[c, h]	45-60[c, g]	28–55[c, g]
Pollen	1–2.5[a]	**0.04–0.30[i, j,m]**	0.16–0.44[i, j, k]	0.5–0.8[i]	−0.5–0.5	38-63[k]	40–72[k]
Dust	0.05–0.45[a]	0.22–0.30[c, l]	0.25–0.35[c, l]	0.3–0.6	−0.3–0.44[c]	40–46[c, l]	35–44[c, h, l]

[a] (Veselovskii et al., 2024). [b](Haarig et al., 2018). [c](Floutsi et al., 2023). [d](De Rosa et al., 2022). [e](De Rosa et al., 2025). [f](Mylonaki et al., 2021). [g](Giannakaki et al., 2016). [h](Che et al., 2015). [i](Shang et al., 2020). [j](Bohlmann et al., 2021). [k](Bohlmann et al., 2019). [l](Hofer et al., 2020). [m](Cholleton et al.,2022). Full references for all sources cited in Table R2 are listed below.

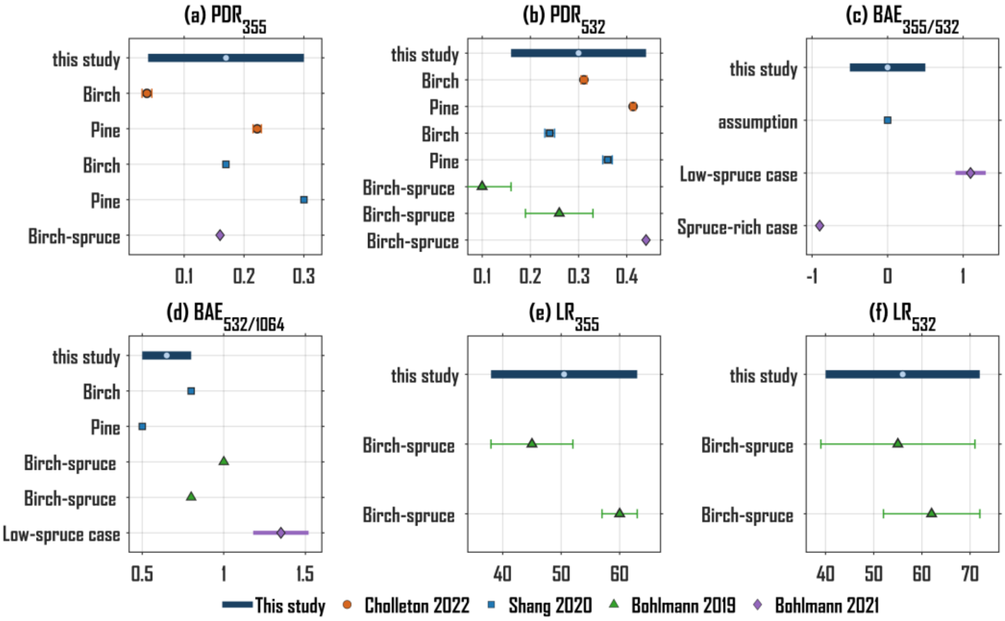

Figure R5. Comparison between the corrected pollen classification ranges used in this study and the cited literature values, including the laboratory birch and pine pollen measurements of Cholleton et al. (2022). The y-axis labels specify the pollen type or observational/laboratory case, and the legend indicates the literature source.

Reference

Bohlmann, S., Shang, X., Giannakaki, E., Filioglou, M., Saarto, A., Romakkaniemi, S., and Komppula, M.: Detection and characterization of birch pollen in the atmosphere using a multiwavelength Raman polarization lidar and Hirst-type pollen sampler in Finland, Atmos. Chem. Phys., 19, 14559-14569, 10.5194/acp-19-14559-2019, 2019.

Bohlmann, S., Shang, X., Vakkari, V., Giannakaki, E., Leskinen, A., Lehtinen, K. E. J., Pätsi, S., and Komppula, M.: Lidar depolarization ratio of atmospheric pollen at multiple wavelengths, Atmos. Chem. Phys., 21, 7083-7097, 10.5194/acp-21-7083-2021, 2021.

Che, H., Xia, X., Zhu, J., Wang, H., Wang, Y., Sun, J., Zhang, X., and Shi, G.: Aerosol optical properties under the condition of heavy haze over an urban site of Beijing, China, Environmental Science and Pollution Research, 22, 1043-1053, 10.1007/s11356-014-3415-5, 2015.

Cholleton, D., Rairoux, P., and Miffre, A.: Laboratory Evaluation of the (355, 532) nm Particle Depolarization Ratio of Pure Pollen at 180.0° Lidar Backscattering Angle, Remote Sensing, 14, 3767, 10.3390/rs14153767, 2022.

De Rosa, B., Amato, F., Amodeo, A., D'Amico, G., Dema, C., Falconieri, A., Giunta, A., Gumà-Claramunt, P., Kampouri, A., Solomos, S., Mytilinaios, M., Papagiannopoulos, N., Summa, D., Veselovskii, I., and Mona, L.: Characterization of Extremely Fresh Biomass Burning Aerosol by Means of Lidar Observations, Remote Sensing, 14, 4984, 10.3390/rs14194984, 2022.

De Rosa, B., Amodeo, A., D'Amico, G., Papagiannopoulos, N., Rosoldi, M., Veselovskii, I., Cardellicchio, F., Falconieri, A., Gumà-Claramunt, P., Laurita, T., Mytilinaios, M., Papanikolaou, C.-A., Amodio, D., Colangelo, C., Di Girolamo, P., Gandolfi, I., Giunta, A., Lapenna, E., Marra, F., Petracca Altieri, R. M., Ripepi, E., Summa, D., Volini, M., Arienzo, A., and Mona, L.: Characterization of Fresh and Aged Smoke Particles Simultaneously Observed with an ACTRIS Multi-Wavelength Raman Lidar in Potenza, Italy, 10.3390/rs17152538, 2025.

Floutsi, A. A., Baars, H., Engelmann, R., Althausen, D., Ansmann, A., Bohlmann, S., Heese, B., Hofer, J., Kanitz, T., Haarig, M., Ohneiser, K., Radenz, M., Seifert, P., Skupin, A., Yin, Z., Abdullaev, S. F., Komppula, M., Filioglou, M., Giannakaki, E., Stachlewska, I. S., Janicka, L., Bortoli, D., Marinou, E., Amiridis, V., Gialitaki, A., Mamouri, R. E., Barja, B., and Wandinger, U.: DeLiAn – a growing collection of depolarization ratio, lidar ratio and Ångström exponent for different aerosol types and mixtures from ground-based lidar observations, Atmos. Meas. Tech., 16, 2353-2379, 10.5194/amt-16-2353-2023, 2023.

Giannakaki, E., van Zyl, P. G., Müller, D., Balis, D., and Komppula, M.: Optical and microphysical characterization of aerosol layers over South Africa by means of multi-wavelength depolarization and Raman lidar measurements, Atmospheric Chemistry and Physics, 16, 8109-8123, 10.5194/acp-16-8109-2016, 2016.

Haarig, M., Ansmann, A., Baars, H., Jimenez, C., Veselovskii, I., Engelmann, R., and Althausen, D.: Depolarization and lidar ratios at 355, 532, and 1064 nm and microphysical properties of aged tropospheric and stratospheric Canadian wildfire smoke, Atmospheric Chemistry and Physics, 18, 11847-11861, 10.5194/acp-18-11847-2018, 2018.

Hofer, J., Ansmann, A., Althausen, D., Engelmann, R., Baars, H., Fomba, K. W., Wandinger, U., Abdullaev, S. F., and Makhmudov, A. N.: Optical properties of Central Asian aerosol relevant for spaceborne lidar applications and aerosol typing at 355 and 532 nm, Atmospheric Chemistry and Physics, 20, 9265-9280, 10.5194/acp-20-9265-2020, 2020.

Mylonaki, M., Giannakaki, E., Papayannis, A., Papanikolaou, C.-A., Komppula, M., Nicolae, D., Papagiannopoulos, N., Amodeo, A., Baars, H., and Soupiona, O.: Aerosol type classification analysis using EARLINET multiwavelength and depolarization lidar observations, Atmospheric Chemistry and Physics, 21, 2211-2227, 10.5194/acp-21-2211-2021, 2021.

Shang, X., Giannakaki, E., Bohlmann, S., Filioglou, M., Saarto, A., Ruuskanen, A., Leskinen, A., Romakkaniemi, S., and Komppula, M.: Optical characterization of pure pollen types using a multi-wavelength Raman polarization lidar, Atmospheric Chemistry and Physics, 20, 15323-15339, 10.5194/acp-20-15323-2020, 2020.

Veselovskii, I., Barchunov, B., Hu, Q., Goloub, P., Podvin, T., Korenskii, M., Dubois, G., Boissiere, W., and Kasianik, N.: Retrieval and analysis of the composition of an aerosol mixture through Mie–Raman–fluorescence lidar observations, Atmos. Meas. Tech., 17, 4137-4152, 10.5194/amt-17-4137-2024, 2024.

7) (c) I am surprise that uncertainty of BAE obtained for 532/1064 is lower than for 355/532. Values at 355 and 532 nm are obtained from Raman measurements, which normally are more accurate than values obtained with Fernald method.

Authors' response:

To avoid misunderstanding, we clarify that the intervals listed in Table S1 are not propagated instrumental, measurement, or retrieval uncertainties. Instead, they are literature-based classification intervals compiled from previously reported aerosol optical properties. Thus, the width of each interval reflects the empirical spread used for aerosol-type separation, not the retrieval precision of the corresponding wavelength pair. In this sense, a narrower $BAE_{532/1064}$ interval does not imply that $BAE_{532/1064}$ is measured more accurately than $BAE_{355/532}$; it only indicates that, for the relevant aerosol class, the literature values adopted in our classification scheme occupy a narrower empirical range.

To avoid ambiguity, we have added the following description of Table S1:

"*The intervals listed in this table are literature-based classification priors used in the Monte Carlo aerosol-type separation. They represent the empirical variability of reported aerosol optical properties for each aerosol class and should not be interpreted as propagated instrumental, measurement, or retrieval uncertainties*."

Reference

Ansmann, A., Wandinger, U., Riebesell, M., Weitkamp, C., and Michaelis, W.: Independent measurement of extinction and backscatter profiles in cirrus clouds by using a combined Raman elastic-backscatter lidar, Appl. Opt., 31, 7113-7131, 10.1364/AO.31.007113, 1992.

Fernald, F. G.: Analysis of atmospheric lidar observations: some comments, Appl. Opt., 23, 652, 10.1364/ao.23.000652, 1984.

8) (d) LR for smoke at 532 nm is normally higher than for 355. Why it is opposite? Should be explained, how the values for pollen were obtained. Usually pollen are mixed with other aerosol types.

Authors' response:

(1) Response to Comment (d): lidar ratio of smoke

We thank the reviewer for this important comment. We agree that the original smoke LR_{532} interval in Table S1 could be misleading and should be revised. For aged or long-range-transported smoke, LR_{532} is generally comparable to or higher than LR_{355}. This relationship has been reported in multiwavelength lidar observations. For example, Haarig et al. (2018) reported higher LR_{532} than LR_{355} for aged Canadian wildfire smoke.

To further check the consistency of our adopted intervals with published lidar statistics, we compared the smoke lidar-ratio ranges with the DeLiAn database (Figure R4). In DeLiAn, the mean smoke LR is 68.2 sr at 355 nm and 71.9 sr at 532 nm, indicating a slightly higher mean value at 532 nm. This comparison supports the reviewer's point that the central tendency of LR_{532} for smoke should not be lower than that of LR_{355}.

Following the reviewer's suggestion and the comparison with previous lidar statistics, especially the DeLiAn database, we revised the smoke LR_{532} interval in Table S1 (Table R2). The original LR_{532} range of 30-85 sr covered an overly broad lower end and was not sufficiently focused around the literature-supported range for aged or transported smoke. Therefore, based on the DeLiAn statistics and the reported tendency that LR_{532} is generally comparable to or slightly higher than LR_{355}, we narrowed the smoke LR_{532} interval from 30-85 sr to 45-85 sr, while keeping the LR_{355} interval at 40-76 sr. After this revision, the adopted smoke lidar-ratio intervals are more concentrated around the previously reported smoke values and better reflect the DeLiAn-supported tendency that LR for smoke at 532 nm is normally comparable to or higher than that at 355 nm.

(2) Response to Comment: pollen values and aerosol mixing.

For the pollen-related parameters, we also agree that atmospheric pollen layers are often mixed with background aerosols and that the derivation of the pollen parameters in Table S1 should be explained more clearly.

In our classification framework, the pollen parameters in Table S1 are intended to approximate the optical properties of representative pollen particles used in the aerosol-type separation. This approximation is based on two complementary types of evidence. The first is pure or controlled pollen measurements, which provide the most direct constraints on the intrinsic optical properties of pollen particles. In particular, Cholleton et al. (2022) measured the particle depolarization ratios of pure pollen at 355 and 532 nm under laboratory conditions, and Shang et al. (2020) reported multiwavelength optical properties of pure birch and pine pollen. These studies provide the main basis for constraining the pollen PDR and BAE intervals.

The second type of evidence is pollen-dominated atmospheric observations, which are especially important for lidar-ratio constraints because direct pure-pollen lidar-ratio measurements are still limited. Bohlmann et al. (2019) combined multiwavelength Raman polarization lidar observations with a Hirst-type pollen sampler, allowing the observed aerosol layers to be linked to independently measured pollen occurrence and dominant taxa. During the birch-dominated period, they reported $LR_{355} = 45 \pm 7$ sr and $LR_{532} = 55 \pm 16$ sr; during the birch-spruce period, they reported $LR_{355} = 60 \pm 3$ sr and $LR_{532} = 62 \pm 10$ sr. These values were used to constrain the pollen LR intervals in Table S1.

Although the atmospheric pollen observations may include background aerosol, they are still useful for defining representative pollen optical properties because the selected periods were identified as pollen-dominated by independent in situ pollen measurements. Therefore, these observations help bridge the gap between pure-pollen laboratory properties and the effective lidar response of pollen under real atmospheric conditions. In this sense, the pollen intervals in Table S1 are reasonable approximations of representative pollen optical properties for the ABLES classification framework.

To clarify this point, we have added the following description of Table S1:

"*The pollen intervals were derived from both pure or controlled pollen measurements and pollen-dominated atmospheric observations. The PDR and BAE intervals are mainly constrained by laboratory or controlled measurements of representative tree pollen, including birch and pine pollen reported by Cholleton et al. (2022) and Shang et al. (2020). The LR intervals are mainly based on pollen-dominated atmospheric observations reported by Bohlmann et al. (2019), where multiwavelength Raman polarization lidar measurements were combined with a Hirst-type pollen sampler to identify pollen occurrence and dominant taxa. Although atmospheric pollen* *layers may contain background aerosols, these pollen-dominated cases provide the best available atmospheric constraints for the effective lidar response of pollen. Therefore, the pollen row in Table S1 is intended to approximate the optical properties of representative pollen particles used in the aerosol-type separation at ABLES.*"

Reference

Bohlmann, S., Shang, X., Giannakaki, E., Filioglou, M., Saarto, A., Romakkaniemi, S., and Komppula, M.: Detection and characterization of birch pollen in the atmosphere using a multiwavelength Raman polarization lidar and Hirst-type pollen sampler in Finland, Atmos. Chem. Phys., 19, 14559-14569, 10.5194/acp-19-14559-2019, 2019

Floutsi, A. A., Baars, H., Engelmann, R., Althausen, D., Ansmann, A., Bohlmann, S., Heese, B., Hofer, J., Kanitz, T., Haarig, M., Ohneiser, K., Radenz, M., Seifert, P., Skupin, A., Yin, Z., Abdullaev, S. F., Komppula, M., Filioglou, M., Giannakaki, E., Stachlewska, I. S., Janicka, L., Bortoli, D., Marinou, E., Amiridis, V., Gialitaki, A., Mamouri, R. E., Barja, B., and Wandinger, U.: DeLiAn – a growing collection of depolarization ratio, lidar ratio and Ångström exponent for different aerosol types and mixtures from ground-based lidar observations, Atmos. Meas. Tech., 16, 2353-2379, 10.5194/amt-16-2353-2023, 2023.

Haarig, M., Ansmann, A., Baars, H., Jimenez, C., Veselovskii, I., Engelmann, R., and Althausen, D.: Depolarization and lidar ratios at 355, 532, and 1064 nm and microphysical properties of aged tropospheric and stratospheric Canadian wildfire smoke, Atmospheric Chemistry and Physics, 18, 11847-11861, 10.5194/acp-18-11847-2018, 2018.

Shang, X., Giannakaki, E., Bohlmann, S., Filioglou, M., Saarto, A., Ruuskanen, A., Leskinen, A., Romakkaniemi, S., and Komppula, M.: Optical characterization of pure pollen types using a multi-wavelength Raman polarization lidar, Atmospheric Chemistry and Physics, 20, 15323-15339, 10.5194/acp-20-15323-2020, 2020.

9) Ln.170. References for previous works, where extinction-to-volume conversion factors were presented, should be cited.

Mamouri, R.-E., and Ansmann, A.: Potential of polarization/Raman lidar to separate fine dust, coarse dust, maritime, and anthropogenic aerosol profiles, Atmos. Meas. Tech., 10, 3403–3427, https://doi.org/10.5194/amt-10-3403-2017, 2017.

He, Y., Yin, Z., Ansmann, A., Liu, F., Wang, L., Jing, D., and Shen, H.: POLIPHON conversion factors for retrieving dust-related cloud condensation nuclei and ice-nucleating particle concentration profiles at oceanic sites, Atmos. Meas. Tech., 16, 1951–1970, https://doi.org/10.5194/amt-16-1951-2023, 2023.

Ansmann, A., Mamouri, R.-E., Hofer, J., Baars, H., Althausen, D., and Abdullaev, S. F.: Dust mass, cloud condensation nuclei, and ice-nucleating particle profiling with polarization lidar: updated POLIPHON conversion factors from global AERONET analysis, Atmos. Meas. Tech., 12, 4849–4865, https://doi.org/10.5194/amt-12-4849-2019, 2019.

Authors' response:

We thank the reviewer for this suggestion. The direct sources of the parameters used in Table 2 were already cited around Line 170 in the original manuscript: "The relevant parameters are listed in Table 2 (Veselovskii et al., 2024; Filioglou et al., 2025)." To make the literature basis clearer, we added additional references on extinction-to-volume conversion factors and revised the corresponding text as follows.

We revised the sentence around Line 170 to include the relevant POLIPHON studies. In addition, to avoid overgeneralizing the applicability of the pollen parameters, we further clarified that the pollen-related conversion parameters used in this study mainly refer to tree-pollen lidar studies, particularly the extinction-to-volume and extinction-to-number conversion factors for birch pollen reported by Filioglou et al. (2025). Veselovskii et al. (2024) supports the overall Mie-Raman-fluorescence lidar framework for aerosol-mixture decomposition. Considering that the ABLES site is surrounded mainly by broadleaf and coniferous forests, the pollen parameters used here should be interpreted as representative approximate values for local tree pollen in this forested environment, mainly constrained by birch-type tree-pollen studies, rather than universal parameters applicable to all pollen species or all regions.

The revised sentence now reads:

"*Here, LR_{532}^{i} represents the lidar ratio of each aerosol type at 532 nm. C_{V}^{i} denotes the extinction-to-volume conversion coefficient used to convert the extinction coefficient into volume concentration, which is then converted into mass concentration using the particle density ρ^{i}. The relevant parameters are listed in Table 2, following previous POLIPHON studies and aerosol-mixture retrieval work (Mamouri and Ansmann, 2017; Ansmann et al., 2019; He et al., 2023; Veselovskii et al., 2024; Filioglou et al., 2025). It should be noted that the pollen-related conversion parameters are mainly constrained by tree-pollen lidar studies, especially the extinction-to-volume and extinction-to-number conversion factors for birch pollen reported by Filioglou et al. (2025). Therefore, the pollen parameters in Table 2 should be interpreted as representative approximate values for local tree pollen around the ABLES site, which is surrounded mainly by broadleaf and coniferous forests, rather than universal parameters for all pollen species or all regions*."

These POLIPHON references have also been added to the reference list. This revision clarifies both the direct sources of the parameter values used in this study, the methodological background of the extinction-to-volume conversion factors, and the applicability and limitations of the pollen parameters.

10) Table 2. Uncertainties for lidar ratios should be provided.

Authors' response:

We have revised Table 2 by reporting the 532 nm lidar ratios as representative values with literature-based uncertainties.

For smoke, urban aerosol, and dust, the lidar ratios were taken from the aerosol-mixture retrieval framework of Veselovskii et al. (2024). In that study, the lidar ratios used for smoke, urban aerosol, and dust were 64, 61, and 45 sr, respectively. Veselovskii et al. (2024) summarized literature ranges of 50-78 sr for aged smoke, 53-70 sr for urban aerosol, and 40-50 sr for dust. In the revised Table 2, we therefore express these values as representative values with half-range uncertainties, namely 64 ± 14 sr for smoke, 61 ± 9 sr for urban aerosol, and 45 ± 5 sr for dust.

For pollen, the lidar-ratio uncertainty is based on atmospheric pollen observations reported by Bohlmann et al. (2019). They combined multiwavelength Raman polarization lidar measurements with a Hirst-type pollen sampler and reported mean 532 nm lidar ratios of 55 ± 16 sr during a birch pollen period and 62 ± 10 sr during a birch-spruce pollen period. Based on these observations, we used 60 ± 16 sr as a representative 532 nm lidar ratio for pollen in this study, where the uncertainty conservatively reflects the larger reported variability. Accordingly, Table 2 has been revised to include lidar-ratio uncertainties for all four aerosol types:

Table R3. Literature-based lidar ratios, extinction-to-volume conversion coefficients, and density values used for the four aerosol types in the mass-concentration retrieval.

Type	LR_{532}	C_V(μm^3 cm^{-3} Mm)	ρ(g cm^{-3})	Source
Smoke	64 ± 14	0.13	1.15	Veselovskii et al. (2024)
Urban	61 ± 9	0.35	1.50	Veselovskii et al. (2024)
Pollen	60 ± 16	1.79	0.80	Bohlmann et al. (2019); Filioglou et al. (2025)
Dust	45 ± 5	0.70	2.60	Veselovskii et al. (2024); Mamouri and Ansmann (2017); Ansmann et al. (2019); He et al. (2023)

Reference

Bohlmann, S., Shang, X., Giannakaki, E., Filioglou, M., Saarto, A., Romakkaniemi, S., and Komppula, M.: Detection and characterization of birch pollen in the atmosphere using a multiwavelength Raman polarization lidar and Hirst-type pollen sampler in Finland, Atmos. Chem. Phys., 19, 14559-14569, 10.5194/acp-19-14559-2019, 2019.

Veselovskii, I., Barchunov, B., Hu, Q., Goloub, P., Podvin, T., Korenskii, M., Dubois, G., Boissiere, W., and Kasianik, N.: Retrieval and analysis of the composition of an aerosol mixture through Mie–Raman–fluorescence lidar observations, Atmos. Meas. Tech., 17, 4137-4152, 10.5194/amt-17-4137-2024, 2024.

11) Section 3.1. Usually ground based lidar measurements are used to validate CALIPSO results. Authors do opposite. I don't think that this is proper validation of their system. Probably section 3.1.1 is not necessary.

Authors' response:

Thank you for this comment. We agree with the reviewer that using CALIPSO to validate a ground-based multiwavelength Raman-fluorescence lidar system is not appropriate. In most cases, high-quality ground-based lidar observations are used to evaluate or validate spaceborne CALIPSO products, rather than the reverse. Therefore, the original presentation of the CALIPSO comparison in Section 3.1.1 as part of "validation" was misleading.

Following the reviewer's suggestion, we revised this part of the manuscript. The CALIPSO comparison is no longer used as validation of the ground-based lidar system or retrieval algorithm. Instead, we moved it to the Supplementary Material and now present it only as an ancillary qualitative consistency check under near-coincident satellite overpass conditions. We also replaced the wording "validation" with more appropriate terms such as "ancillary comparison" and "qualitative consistency check".

In the revised manuscript, Section 3.1 now focuses on comparisons with independent observations that are more suitable for evaluating the retrieval results, including UAV-based bioaerosol measurements for the fluorescence-derived particle profiles and ground-level $PM_{2.5}$/PM_{10} observations for the bottom-layer aerosol mass concentrations. These datasets provide more direct observational constraints than CALIPSO for the purpose of evaluating the ground-based lidar retrievals.

12) Ln.225. Fluorescence is provided not only by bioaerosols, but also by secondary organic particles. So particles number can be obtained from Eq.10 only for very special situations. Besides, fluorescence cross section of biological particles varies in a wide range.

Authors' response:

Thank you for this important comment. The revised manuscript now clarifies that aerosol fluorescence is not unique to biological particles. In addition to primary biological aerosol particles (PBAPs), secondary organic aerosol (SOA), humic-like substances (HULIS), brown carbon, aged combustion-related organic aerosol, and other organic particles may also fluoresce under UV excitation. Previous laboratory and field studies have shown that non-biological organic aerosol components, including SOA, HULIS, and brown-carbon-related chromophores, can contribute to aerosol fluorescence signals under certain atmospheric conditions (Pöhlker et al., 2012; Zhang et al., 2021; Yue et al., 2022; Jiang et al., 2022).

In the revised manuscript, we clarified that Eq. (10) should not be interpreted as a strict source-specific retrieval of the true bioaerosol number concentration. Instead, Eq. (10) is used as a semi-quantitative conversion from fluorescence backscatter to a bioaerosol-equivalent fluorescence-derived number concentration. This term emphasizes that the retrieved value is an apparent equivalent concentration inferred from the total fluorescence backscatter by using an effective biological-particle fluorescence cross section, rather than a number concentration that excludes all possible non-biological fluorescent contributions. This formulation makes Eq. (10) more appropriate for the purpose of this study. The equation provides a first-order fluorescence-based equivalent metric that can be compared with UAV observations in terms of magnitude and vertical structure, while explicitly acknowledging that part of the fluorescence signal may originate from SOA/HULIS/BrC-related organic aerosol components. In particular, wintertime aerosol fluorescence studies have reported that HULIS-like and brown-carbon-related chromophores can make substantial contributions to resolved aerosol fluorescence or chromophoric organic matter (Jiang et al., 2022; Zhong et al., 2023). These findings support the need to treat non-biological fluorescent organic aerosol as an important uncertainty source in the interpretation of Eq. (10).

Accordingly, we revised the wording in the manuscript to avoid presenting Eq. (10) as a strict retrieval of true bioaerosol number concentration. We now describe the result as a bioaerosol-equivalent fluorescence-derived number concentration and explicitly state that SOA, HULIS, brown carbon, and other non-biological fluorescent organic components may cause a positive bias in this semi-quantitative estimate.

Revised text after Eq. (10) (Lines 225-232):

"Here, σ_{bio}^{F} *represents the effective fluorescence cross section of biological aerosol particles, adopted as 10-11 cm2 sr-1 nm-1 following Rao et al. (2018), and Δλ denotes the bandwidth of the fluorescence channel filter, i.e., 44 nm. It should be noted that Eq. (10) gives a bioaerosol-equivalent fluorescence-derived number concentration, meaning that the observed fluorescence backscatter is converted into an equivalent number concentration using an effective biological-particle fluorescence cross section. This value should not be interpreted as the true bioaerosol number concentration, because aerosol fluorescence can also originate from non-biological organic components such as SOA, HULIS, and brown carbon (Pöhlker et al., 2012; Zhang et al., 2021; Yue et al., 2022; Jiang et al., 2022), and the fluorescence cross section of biological aerosols can vary with species, particle size, hydration state, aging, excitation wavelength, and detection band (Manninen et al., 2009; Pan, 2015). Therefore, Eq. (10) is used here as a semi-quantitative fluorescence-based equivalent metric for comparison with UAV observations in terms of magnitude and vertical structure."*

References

Jiang, F., Song, J., Bauer, J., Gao, L., Vallon, M., Gebhardt, R., Leisner, T., Norra, S., and Saathoff, H.: Chromophores and chemical composition of brown carbon characterized at an urban kerbside by excitation–emission spectroscopy and mass spectrometry, Atmos. Chem. Phys., 22, 14971–14986, https://doi.org/10.5194/acp-22-14971-2022, 2022.

Manninen, A., Putkiranta, M., Saarela, J., Rostedt, A., Sorvajärvi, T., Toivonen, J., Marjamäki, M., Keskinen, J., and Hernberg, R.: Fluorescence cross sections of bioaerosols and suspended biological agents, Appl. Opt., 48, 4320-4328, 10.1364/AO.48.004320, 2009.

Pan, Y.-L.: Detection and characterization of biological and other organic-carbon aerosol particles in atmosphere using fluorescence, Journal of Quantitative Spectroscopy and Radiative Transfer, 150, 12-35, https://doi.org/10.1016/j.jqsrt.2014.06.007, 2015.

Pöhlker, C., Huffman, J. A., and Pöschl, U.: Autofluorescence of atmospheric bioaerosols – fluorescent biomolecules and potential interferences, Atmos. Meas. Tech., 5, 37–71, https://doi.org/10.5194/amt-5-37-2012, 2012.

Rao, Z., He, T., Hua, D., Wang, Y., Wang, X., Chen, Y., and Le, J.: Preliminary measurements of fluorescent aerosol number concentrations using a laser-induced fluorescence lidar, Appl. Opt., 57, 7211-7215, 10.1364/AO.57.007211, 2018.

Yue, S., Li, L., Xu, W., Zhao, J., Ren, H., Ji, D., Li, P., Zhang, Q., Wei, L., Xie, Q., Pan, X., Wang, Z., Sun, Y., and Fu, P.: Biological and nonbiological sources of fluorescent aerosol particles in the urban atmosphere, Environ. Sci. Technol., 56, 7588–7597, https://doi.org/10.1021/acs.est.1c07966, 2022.

Zhang, M., Su, H., Li, G., et al.: High-resolution fluorescence spectra of airborne biogenic secondary organic aerosols: comparisons to primary biological aerosol particles and implications for single-particle measurements, Environ. Sci. Technol., 55, 16747–16756, https://doi.org/10.1021/acs.est.1c02536, 2021.

Zhong, M., Xu, J., Wang, H., Gao, L., Zhu, H., Zhai, L., Zhang, X., and Zhao, W.: Characterizing water-soluble brown carbon in fine particles in four typical cities in northwestern China during wintertime: integrating optical properties with chemical processes, Atmos. Chem. Phys., 23, 12609–12630, https://doi.org/10.5194/acp-23-12609-2023, 2023.

13) I have difficulty to understand scales in Fig.3d. White spots on green background. How can I get numbers from them? Why authors don't show lidar measured profiles?

Authors' response:

To improve the readability of Fig. 3d, we revised the colormap so that corresponding values can be read more directly from the colorbar (Figure R6). Based on the updated figure, the peak bioaerosol number concentration during the before period (00:00-07:00 LST on 11 December 2025) is approximately 4.42 × 10^5 particles m^{-3}, whereas during the after period (18:00-23:00 LST) it reaches approximately 6.37 × 10^7 particles m^{-3}. The revised color scale therefore makes the magnitude contrast between the two periods much easier to interpret quantitatively.

Regarding the reviewer’s question on 'lidar measured profiles', we agree that the measurement basis of the retrieval should be shown more explicitly. Since the final bioaerosol number concentration is obtained from the fluorescence backscatter through a simple proportional conversion, adding another profile of the derived bioaerosol product alone would not provide substantial independent information. Instead, we have added supplementary vertical profiles of the key lidar-measured/retrieved variables directly used in the retrieval, including the range-squared-corrected fluorescence signal, the range-squared-corrected Raman signal, and the 532 nm extinction profile used for transmission correction. These profiles provide a more direct representation of the lidar measurement basis underlying Figure R6(d).

Overall, we revised Fig. 3d to improve the readability of the color scale and added the relevant lidar-based vertical profiles in the Supplementary Material, so that both the quantitative values and the observational basis of the retrieval are now more clearly documented.

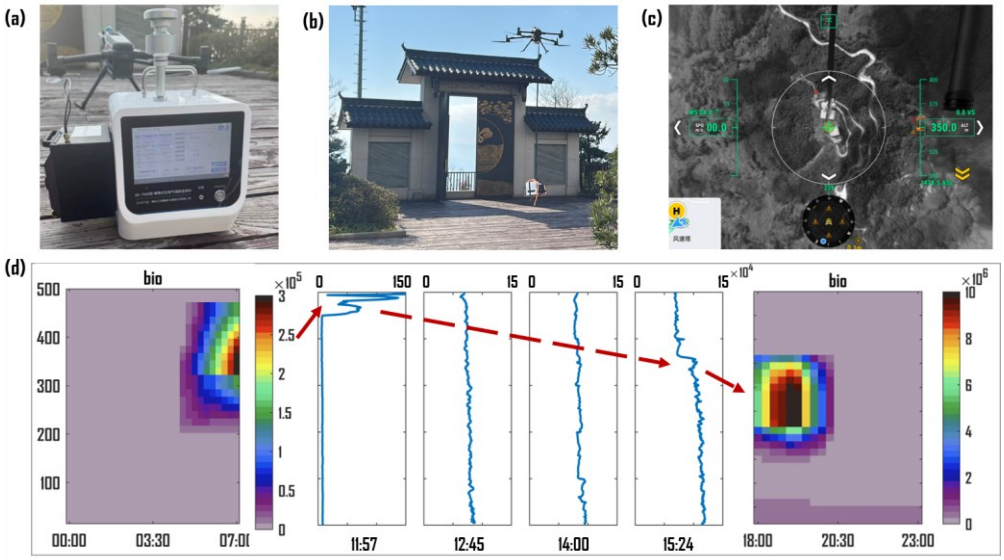

Figure R6. UAV-based validation experiment and diurnal bioaerosol profiling. (a) ZR-7500 bioaerosol instrument. (b) On-site photograph of the UAV operation at ABLES. (c) Aerial image from the flight. (d) Vertical profiles of bioaerosol number concentration on 11 December 2025, showing the temporal connection between daytime UAV data and nighttime lidar retrievals.

14) Ln.241 Need to explain how they obtained $PM_{2.5}$ *and* PM_{10} *values.*

Authors' response:

We thank the reviewer for pointing this out. The $PM_{2.5}$ and PM_{10} values used in this study were obtained from collocated ground-based in-situ particulate matter observations at the ABLES site.

$PM_{2.5}$ and PM_{10} were measured using a Thermo Scientific Model 5014i continuous ambient particulate monitor equipped with $PM_{2.5}$ and PM_{10} size cut-off inlets before the sampling inlet. The original observations were recorded at 1 min resolution and were averaged to the corresponding lidar retrieval time intervals before comparison with the retrieved aerosol mass concentrations.

We have revised the manuscript around Line 241 to clarify the source of the $PM_{2.5}$ and PM_{10} data, the instrument used, and the temporal matching procedure.

Revised text around Line 241:

"*The ground-based* $PM_{2.5}$ *and* PM_{10} *mass concentrations used for validation were obtained from collocated in-situ particulate matter measurements at the ABLES site.* $PM_{2.5}$ *and* PM_{10} *were measured using a Thermo Scientific Model 5014i continuous ambient particulate monitor equipped with* $PM_{2.5}$ *and* PM_{10} *size cut-off inlets before the sampling inlet. The original 1 min observations were averaged to the corresponding lidar retrieval time intervals before comparison with the retrieved aerosol mass concentrations.*"

15) Ln. 247. 'While winter retrievals achieve the highest accuracy due to low aerosol loading...' For me it sounds strange, because it is very difficult to obtain particle parameters for low scattering ratio.

Authors' response:

Thank you for pointing this out. We agree that the original statement that winter retrievals achieved the highest accuracy 'due to low aerosol loading' was not sufficiently rigorous and could be misleading. In fact, under low aerosol loading or low scattering-ratio conditions, the aerosol optical signal is weak and retrieval of particle parameters is usually more challenging. Therefore, low aerosol loading should not be presented as a direct cause of higher retrieval accuracy.

We have removed this causal interpretation and revised the discussion more cautiously. The revised text only states that winter samples are mainly concentrated in a relatively low-concentration regime and remain generally close to the 1:1 line within that range, without attributing the agreement to low aerosol loading itself. The revised wording is as follows:

"Regarding seasonal characteristics, the retrieval performance exhibits clear seasonal variability. Winter samples are mainly concentrated in a relatively low-concentration regime and remain generally close to the 1:1 line, indicating acceptable agreement within this range. However, this does not mean that low aerosol loading improves retrieval accuracy; on the contrary, particle-parameter retrievals are generally more challenging under low-scattering-ratio conditions. Spring shows the largest scatter, likely associated with complex aerosol mixtures, especially the coexistence of dust, pollen, and other aerosol types. Autumn covers a higher concentration range, likely reflecting transport and/or accumulation processes, while the retrieval still maintains robust consistency under these elevated loading conditions."

In addition, because of the retrieval-algorithm update, the comparison of in situ observations with bottom-layer retrieved mass concentrations at ABLES for $PM_{2.5}$ and PM_{10} has been revised and is now shown as Figure R7.

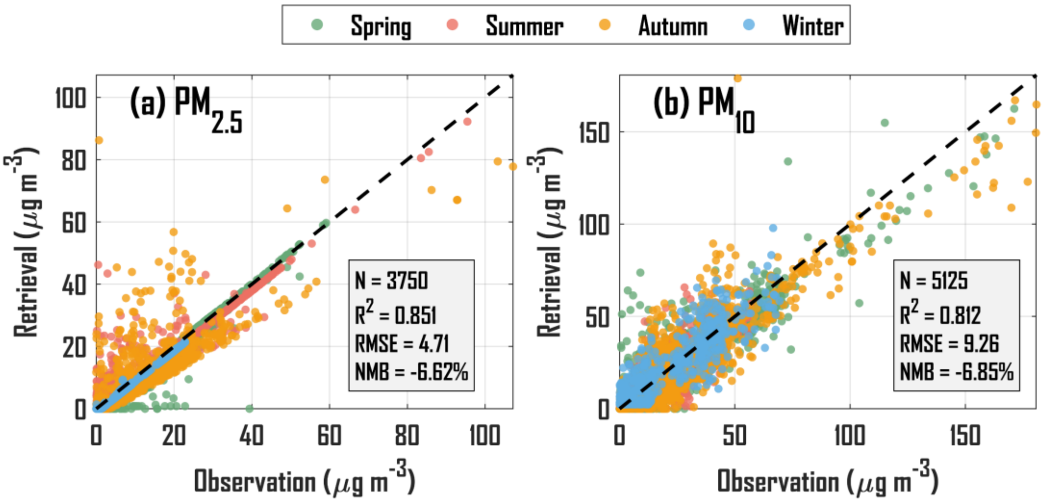

Figure R7. Comparison of in situ observations with bottom-layer retrieved mass concentrations at ABLES after the retrieval-algorithm update for (a) $PM_{2.5}$ and (b) PM_{10}.

16) Section 3.2. Decomposition of aerosol mixture components demands high quality lidar measurements. I would suggest authors to choose several characteristic episodes and to provide lidar measured profiles of all parameters together with results of concentration retrievals. That would help reader to understand how different parameters contribute to aerosol classification.

Authors' response:

We agree that the decomposition of aerosol mixture components requires high-quality multiwavelength Raman/polarization/fluorescence lidar measurements. Statistical results or final classification products alone are not sufficient to show how different optical parameters contribute to the aerosol-type separation. Therefore, in the revised manuscript, we added two representative nighttime case studies, in which the lidar-derived optical parameters, retrieved mass concentrations of the four aerosol components, and ERA5 meteorological fields are presented together.

We selected the nighttime episodes of 3 June 2023 and 7 September 2023 for detailed analysis (Figures R8-R11). The selection was based on three considerations. First, both events occurred at night, when the Raman and fluorescence signals have higher signal-to-noise ratios and the multi-parameter retrieval is more reliable. Second, both events show well-defined aerosol layers within the 0-2 km height range, which allows a direct comparison between the measured optical-parameter fields and the retrieved concentration fields. Third, the two events represent different mixed-aerosol conditions. The 3 June event is mainly characterized by a low-level mixed aerosol layer within a stable nocturnal boundary layer, whereas the 7 September event shows a more vertically stratified mixed-aerosol structure. These contrasting cases are therefore suitable for illustrating how the multi-parameter classification framework reduces aerosol-type ambiguity under realistic mixed conditions.

For the 3 June event, the ERA5 meteorological fields shown in Figure R9 indicate a stable nighttime structure, with temperature decreasing smoothly with height, weak near-surface horizontal wind, and an enhanced wind-speed layer around 1.0-1.5 km. These conditions favor low-level aerosol retention while also suggesting possible regional transport above the surface layer. The vertical velocity is weak overall, indicating that the event is not primarily driven by strong convective vertical transport. The lidar observations in Figure R8 show enhanced β_{532} below about 0.6 km during 20:00-21:00 LST, indicating a pronounced low-level aerosol layer. At the same time, enhanced δ_{355} and δ_{532} indicate the presence of nonspherical particles, while enhanced G_f suggests fluorescent aerosol components. The color ratios $Cr_{1064/532}$ and $Cr_{532/355}$, together with LR_{355} and LR_{532}, further indicate changes in particle-size-related spectral behavior and scattering/absorption properties. The retrieved mass concentrations in Figure R8 show that urban aerosol, dust, and pollen all contribute to the low-level layer, whereas smoke contributes only weakly. This case therefore demonstrates that the enhanced backscatter cannot be interpreted as a single aerosol type, but must be decomposed using the combined constraints from fluorescence, depolarization, color ratio, lidar ratio, and aerosol loading.

For the 7 September event, the meteorological background shown in Figure R11 differs from that on 3 June. Although the temperature field also indicates a stable nocturnal structure, the relative humidity is generally higher, especially within the 1.0-2.0 km layer. The horizontal wind is enhanced around 1.0-1.5 km, and a weak upward-motion signal appears around 21:00 LST, suggesting a more layered transport environment. Correspondingly, the lidar observations in Figure R10 show a more vertically stratified aerosol structure. Around 23:30-00:30 LST, enhanced β_{532} appears at about 0.3-0.7 km, indicating an aerosol layer with increased loading. This layer is accompanied by enhanced G_f, elevated depolarization ratios, and distinct color-ratio structures, indicating a mixture of fluorescent and nonspherical particles with variable particle-size characteristics. The retrieved concentrations in Figure R10 show clear enhancements of pollen and dust in this layer, together with a weaker smoke contribution and relatively weak urban aerosol. Later in the night, weak smoke, pollen, and dust signals also appear around 1.5-1.8 km, suggesting a possible transported layer aloft. This case therefore illustrates a more vertically stratified mixed-aerosol condition than the 3 June case.

A parallel comparison of the two events further highlights the role of different parameters in the classification. β_{532} identifies the height and intensity of aerosol layers, but it cannot determine aerosol type by itself. The depolarization ratios provide information on particle nonsphericity, but pollen and dust may both show enhanced depolarization, leading to ambiguity if depolarization is used alone. G_f provides an additional constraint on fluorescent aerosol components and is particularly useful for identifying pollen-related particles. The color ratios $Cr_{1064/532}$ and $Cr_{532/355}$ constrain the spectral dependence of backscatter and thus provide particle-size-related information. The lidar ratios LR_{355} and LR_{532} add constraints related to scattering and absorption properties. Therefore, the retrieved aerosol components are not determined by a single threshold parameter; rather, they are obtained from the joint constraints of backscatter intensity, fluorescence capacity, depolarization, color ratios, and lidar ratios.

Accordingly, we have added a detailed discussion of these two case studies in the revised Section 3.3. Figures R8 and R10 present the lidar-derived optical parameters together with the retrieved mass concentrations for the 3 June and 7 September events, respectively, while Figures R9 and R11 show the corresponding ERA5 meteorological fields. This new section explains how the meteorological background, optical-parameter responses, and concentration retrievals jointly support the aerosol mixture decomposition and help readers understand how different lidar parameters contribute to aerosol classification.

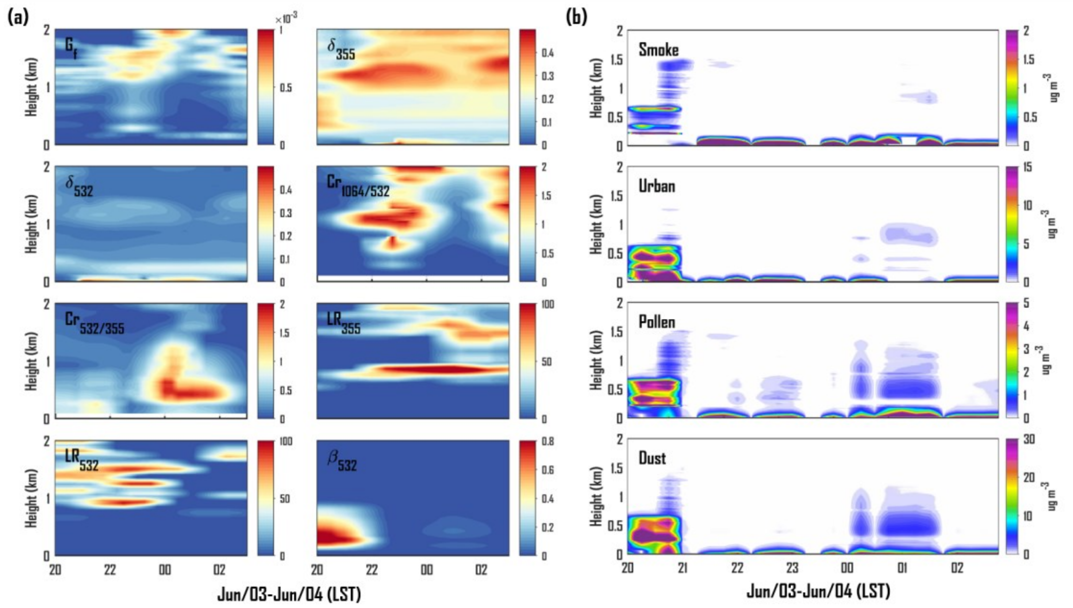

Figure R8. Time-height cross sections of (a) seven lidar-derived optical parameters together with β_{532} and (b) retrieved mass concentrations of the four aerosol components during the nighttime episode from 3 to 4 June 2023.

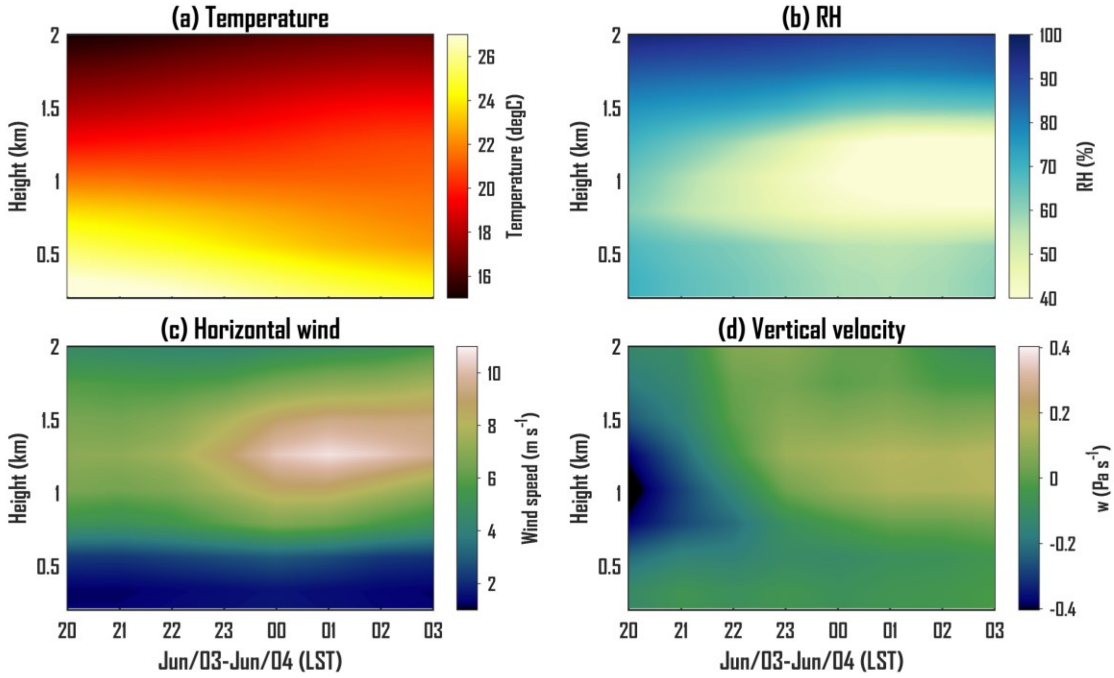

Figure R9. Time-height cross sections of ERA5 meteorological variables during the nighttime episode from 3 to 4 June 2023.

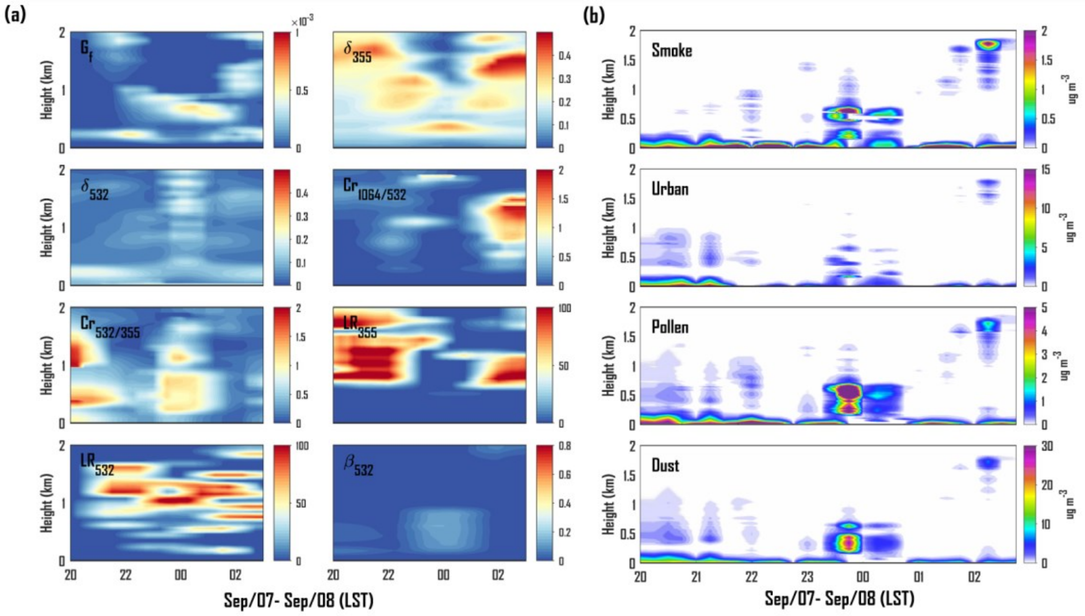

Figure R10. Time-height cross sections of (a) seven lidar-derived optical parameters together with β_{532} and (b) retrieved mass concentrations of the four aerosol components during the nighttime episode from 7 to 8 September 2023.

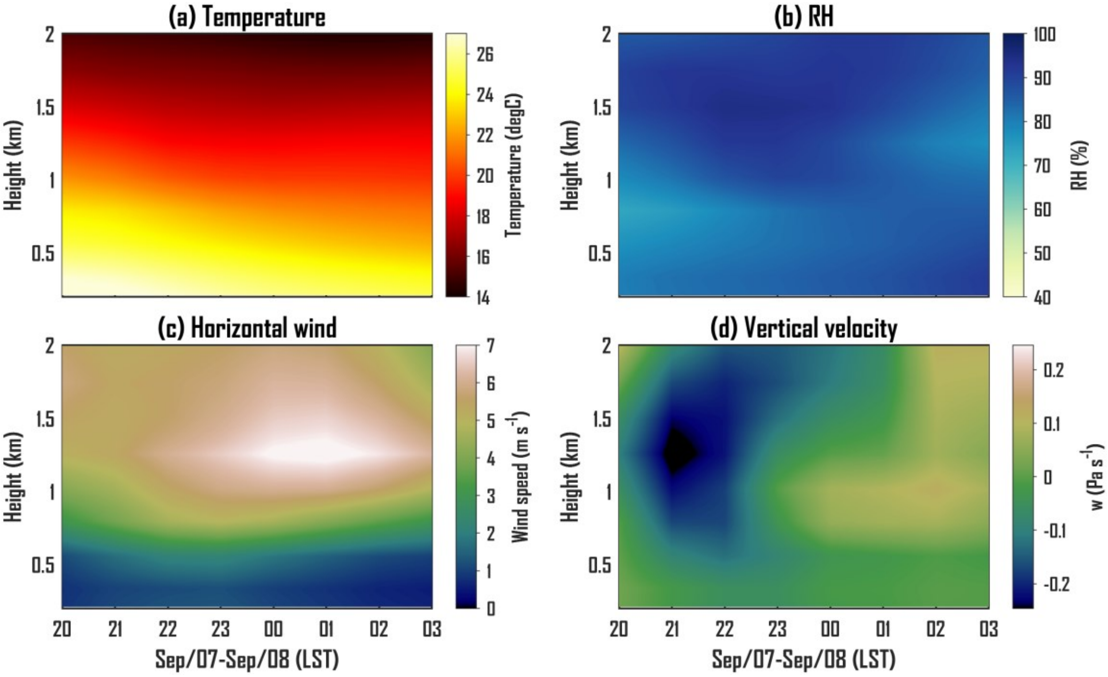

Figure R11. Time-height cross sections of ERA5 meteorological variables during the nighttime episode from 7 to 8 September 2023.